Thermodynamics of mono- and di-vacancies in barium titanate

Paul Erhart[a] and Karsten Albe
Institut für Materialwissenschaft, Technische Universität Darmstadt, Petersenstrasse 23, D-64287 Darmstadt, Germany

(Received 5 May 2007; accepted 1 September 2007; published online 30 October 2007)

The thermodynamic and kinetic properties of mono- and di-vacancy defects in cubic (para-electric) barium titanate $BaTiO_3$ are studied by means of density-functional theory calculations. It is determined which vacancy types prevail for given thermodynamic boundary conditions. The calculations confirm the established picture that vacancies occur in their nominal charge states almost over the entire band gap. For the dominating range of the band gap the di-vacancy binding energies are constant and negative. The system, therefore, strives to achieve a state in which, under metal-rich (oxygen-rich) conditions, all metal (oxygen) vacancies are bound in di-vacancy clusters. The migration barriers are calculated for mono-vacancies in different charge states. As oxygen vacancies are found to readily migrate at typical growth temperatures, di-vacancies can be formed at ease. The key results of the present study with respect to the thermodynamic behavior of mono- and di-vacancies influence the initial defect distribution in the ferroelectric phases and therefore the conditions for aging. © *2007 American Institute of Physics*. [DOI: 10.1063/1.2801011]

I. INTRODUCTION

Barium titanate is a prototypical ferroelectric material. At ambient pressure and temperatures above 393 K it assumes a para-electric, cubic perovskite structure. At lower temperatures a tetragonal distortion of the unit cell is observed which gives rise to ferroelectricity. At even lower temperatures further symmetry reductions lead to ferroelectric orthorhombic and rhombohedral phases. The sequence of phase transitions is the result of subtle structural and energetic differences.[1–4] Probably the most important technological application of barium titanate is in thin-film capacitors.[5] It also serves as an end member in several lead-free ferroelectric alloys,[6] and is used in combination with $SrTiO_3$ to obtain tunable rf devices.[7] Because of its technological importance and its standing as a prototypical ferroelectric, barium titanate has been intensively investigated both experimentally and theoretically.

Intrinsic and extrinsic point defects are of special importance in semiconductors as they control, to a great extent, the electronic properties of these materials. In case of barium titanate, this has motivated a considerable number of studies which used conductivity[5,8–13] and diffusivity[13,14] measurements to infer information about the point defect equilibria in this material. It is further assumed that oxygen vacancies play a key role in aging and fatigue of ferroelectric materials by impeding domain wall motion or by acting as local disturbances of the polarization (see e.g., Refs. 15–19). For this reason, oxygen vacancies and their associates have been intensively studied experimentally (see e.g., Refs. 20–22) as well as theoretically (see e.g., Refs. 23–32).

Experimental investigation of point defect properties, however, are usually restricted in that they either provide bulk information (e.g., conductivity, diffusivity), which corresponds to a macroscopic average over the sample and is therefore defect unspecific, or very localized information (e.g., electron spin resonance, positron annihilation spectroscopy), which is, however, restricted to certain charge states (unpaired spin states) or types of defects (open volumes, vacancies).[33] In general, the correlation between experimental data and specific defects is indirect and therefore potentially ambiguous. Quantum mechanical calculations, on the other hand, are capable of providing a very detailed picture of individual defects and simultaneously sample a whole variety of both different configurations and charge states. They are therefore a very powerful tool for verifying model assumptions and for providing fundamental insights into the energetics of defects as well as their kinetic and electronic properties.

The purpose of the present work is twofold. First, we aim to verify the defect models which have been employed to explain the experimental observations (in particular, conductivity and diffusivity measurements). Second, we explore the formation of di-vacancies which—as argued earlier—is an important ingredient for understanding the deterioration of ferroelectric switchability. The calculations are carried out for the cubic phase, which is the most stable phase at high temperatures where most ceramics are processed and where the initial defect distributions are installed.

II. METHODOLOGY

A. Computational setup

Calculations were carried out within density–functional theory (DFT) using the Vienna *ab initio* simulation package[39–42] in combination with the projector-augmented wave method to represent the ionic cores and core electrons.[43,44] In order to find the most suitable representation for the exchange-correlation functional preliminary calculations were performed within the local-density approxi-

[a]Current address: Lawrence Livermore National Laboratory, Chemistry, Materials and Life Sciences Directorate, L-367, Livermore, CA 94550. Electronic mail:paul.erhart@web.de

TABLE I. Bulk properties of cubic barium titanate as obtained from experiment and first-principles calculations. U.S.-PP: ultrasoft pseudopotentials; FP-LAPW: full potential-linearized augmented plane waves; TB-LMTO: tight-binding linear muffin-tin orbitals; ASA: atomic sphere approximation; LDA: local-density approximation; GGA: generalized-gradient approximation; PBE: Perdew-Burke-Ernzerhof parameterization of the GGA; E_c: cohesive energy (eV/f.u.); a_0: lattice constant (Å); V_0: equilibrium volume (Å^3/f.u.); B, B': bulk modulus (GPa) and its pressure derivative; $E_G^{\Gamma-\Gamma}$: direct band gap at Γ-point (eV); $E_G^{R-\Gamma}$: indirect band gap measured between points R and Γ; m_e^*, m_h^*: effective electron (hole) mass at the Γ-point along ⟨100⟩ in units of the electron mass.

		DFT (Literature)			DFT (This work)						
		Ref. 34 U.S.-PP GGA	Ref. 35 FP-LAPW LDA	Ref. 35 FP-LAPW GGA	Ref. 36 TB-LMTO ASA, LDA	GG-PBE Ti	GG-PBE Ti 3p	GG-PBE Ti 33s-3p	LDA Ti	LDA Ti 3p	LDA Ti 3s-3p
Expt.											
E_c	−31.57[a]	−37.92				−39.62	−39.98	−40.06	−43.84	−44.10	−44.11
a_0	3.992	4.006	3.9	4.0		4.038	4.037	4.038	3.957	3.953	3.955
V_0		64.28	61.0	62.5–65.2		65.84	65.79	65.84	61.98	61.79	61.86
B	173[b]	168	146	185–189		165	161	160	200	194	193
B'		4.5[c]				4.7	4.5	4.5	4.7	4.6	4.6
$E_G^{\Gamma-\Gamma}$	3.27, 3.38[d]		1.8	1.85–1.9	1.2[e]	1.69	1.81	1.85	1.68	1.80	1.82
$E_G^{R-\Gamma}$						1.56	1.66	1.69	1.62	1.71	1.73
m_e^*						1.16	1.16	1.16	1.01	1.00	1.01
						16.7	15.8	15.6	13.5	12.8	12.7
m_h^*						0.96	0.97	0.97	0.89	0.89	0.89
						3.24	3.31	3.32	2.88	2.93	2.94

[a]As cited in Ref. 34.
[b]As cited in Ref. 35.
[c]Fitted to Rose's equation of state (Ref. 37).
[d]Reference 38, obtained from optical measurements on tetragonal barium titanate at room temperature.
[e]At the experimental lattice constant.

mation (LDA),[45,46] as well as the generalized-gradient approximation (GGA) in the Perdew–Burke–Ernzerhof parameterization.[47] We further considered the effect of treating the Ti 3s and Ti 3p electrons as semicore states. All calculations were carried out with 20 k points for Brillouin zone sampling and a plane wave cutoff energy of 500 eV. For each setup the energy-volume curve of cubic barium titanate was computed and the equilibrium lattice constant, cohesive energy, bulk modulus and its pressure derivative were subsequently obtained from a fit to the Birch–Murnaghan equation of state. Finally, the full band diagrams were calculated at the respective zero pressure lattice constant.

The results of these preparatory calculations are compiled in Table I in comparison with experimental and theoretical data from literature. The influence of the Ti 3p and Ti 3s states on the properties included in this comparison is very small. The most significant difference is the increase of the cohesive energies by about 1% upon inclusion of the Ti 3s and Ti 3p electrons in the valence. Thus, while for some properties the deep Ti 3s and Ti 3p can play a crucial role, in the present context their effect is expected to be small. For the sake of computational efficiency we did, therefore, not include the Ti 3s and Ti 3p electrons in the valence.

The exchange-correlation functional, on the other hand, has a more pronounced impact. Within the GGA the bulk modulus is reasonably well reproduced, but the lattice constant is overestimated while the opposite applies for the LDA results. These findings are consistent with the results of previous studies.[34,48,49] In the present study we have decided to employ the LDA.

In order to determine the properties of the phases in Table II we have employed the same computational settings as for $BaTiO_3$ but varied the number of k points for each

TABLE II. Bulk properties of Ba, Ti and O and their compounds in their respective ground-states. Experimental data from Refs. 64–66. E_c: cohesive energy (eV/atom); c/a: axial ratio; r_0: dimer bond length (Å); ΔH_f: enthalpy of formation (eV/f.u.); other symbols as in Table I.

	Experiment	This work
Ba, body-centered cubic ($Im\bar{3}m$, no. 229, A2)		
E_c	−1.87, −1.90	−1.12
a_0	5.020	4.770
B	10	5.3
Ti, hexagonal-close packed ($P6_3/mmc$, no. 194, A3)		
E_c	−4.85	−8.53
a_0	2.950	2.852
c/a	1.588	1.585
B	110	133
O, dimer		
E_c	−2.583	−4.79
r_0	1.21	1.22
BaO, cesium chloride ($Pm\bar{3}m$, no. 221, B2)		
ΔH_f	−5.68	−6.68
a_0	5.496	3.281
B		96
BaO_2 ($I4/mmm$, no. 139, $C11_b$)		
ΔH_f		+0.95
a_0	3.78–3.81	3.768
c/a	1.79	1.783
B		44
TiO_2, rutile ($P4_2/mnm$, no. 139, C4)		
ΔH_f	−9.78	−10.93
a_0	4.594	4.572
c/a	0.644	0.640
B	210	242
$BaTiO_3$, cubic perovskite ($Pm\bar{3}m$, no. 221, $E2_1$)		
ΔH_f	−20.84	−19.83
a_0	3.996	3.957
B	162, 167	200

TABLE III. Formation energies of mono- and di-vacancies under the chemical conditions indicated in Fig. 1. Note that if $\Delta\mu_{Ba}$ and $\Delta\mu_{Ti}$ are given $\Delta\mu_O$ is uniquely determined by Eq. (4). The charge state, q, of the defect which determines the Fermi level dependence of the formation energies via Eq. (1) is given in the second column. The number of electrons occupying conduction band states (n_e) and holes occupying valence band states (n_h) are relevant for the band gap correction via Eq. (2) and are given in the third column where positive and negative values indicate n_h and $-n_e$, respectively. All energies are given in units of eV. The finite-size scaling extrapolation error is given in the last column.

Defect	q	$n_{e,h}$	X	A	C	D	Error
$\Delta\mu_{Ba}$			−4.78	−0.10	−8.90	−6.68	
$\Delta\mu_{Ti}$			−6.02	0.00	−10.93	−13.15	
$\Delta\mu_O$			−3.01	−6.58	0.00	0.00	
V_O	0	−2	5.21	1.64	8.22	8.22	(0.07)
	+1	−1	2.08	−1.49	5.09	5.09	(0.14)
	+2	0	−1.50	−5.07	1.51	1.51	(0.08)
V_{Ba}	−2	+2	5.94	10.61	1.82	4.04	(0.05)
	−1	+1	5.68	10.36	1.56	3.78	(0.03)
	0	0	5.57	10.25	1.45	3.67	(0.02)
$V_{Ba}-V_O$	−2	−2	10.97	12.08	9.86	12.08	(0.14)
	−1	−1	7.26	8.37	6.15	8.37	(0.14)
	0	0	3.83	4.94	2.72	4.94	(0.13)
	+1	+1	3.77	4.88	2.66	4.88	(0.11)
V_{Ti}	−4	0	9.33	15.35	4.42	2.19	(0.15)
	−3	+1	8.92	14.94	4.01	1.79	(0.10)
	−2	+2	8.69	14.71	3.78	1.56	(0.11)
	−1	+3	8.56	14.58	3.65	1.42	(0.08)
	0	+4	8.53	14.55	3.62	1.40	(0.07)
$V_{Ti}-V_O$	−4	−2	13.24	15.70	11.35	9.12	(0.22)
	−3	−1	9.46	11.91	7.56	5.34	(0.22)
	−2	0	5.91	8.37	4.01	1.79	(0.21)
	−1	+1	5.70	8.16	3.80	1.58	(0.13)
	0	+2	5.64	8.10	3.74	1.52	(0.12)
	+1	+3	5.66	8.12	3.76	1.54	(0.10)

material such as to ensure a convergence of the total energy better than 1 meV/unit cell. Energy–volume curves were calculated for each of these structures allowing for full internal relaxation.

B. Defect calculations

1. Formation energies

The formation energy ΔE_D^f of a defect in charge state q is given by[50–53]

$$\Delta E_D^f = (E_D - E_H) + q(E_{VBM} + E_F) - \sum_i \Delta n_i \mu_i, \quad (1)$$

where E_D is the total energy of the defective system and E_H is the total energy of the perfect reference cell. The second term describes the dependence on the Fermi level, E_F, where E_{VBM} is the position of the valence band maximum. The variation of the formation energy with the chemical potentials of the constituents is given by the last term. The difference between the number of atoms of type i in the reference cell with respect to the defective cell is denoted by Δn_i. The chemical potential μ_i of constituent i can be rewritten as $\mu_i = \mu_i^{bulk} + \Delta\mu_i$ where μ_i^{bulk} denotes the chemical potential of the standard reference state and is equivalent to the cohesive energy per atom (see Sec. III B).

For the defect calculations we employed supercells with 40, 60, 90, and 135 atoms equivalent to $2\times2\times2$ to $3\times3\times3$ unit cells. The formation energies given in Table III were obtained by extrapolating the data calculated for different supercell sizes to infinite dilution (see below). We considered both mono-vacancies (V_O, V_{Ba}, V_{Ti}) as well as nearest-neighbor di-vacancies ($V_{Ba}-V_O$, $V_{Ti}-V_O$) taking into account a variety of charge states (see Table III). Due to their size, it is reasonable to assume that host metal ion interstitials have very large formation energies. This assumption is supported by analytical potential calculations which have found Frenkel defects to have much higher energies than Schottky defects.[54] In order to confirm these results we also calculated the formation energies of all interstitials and antisites in the neutral charge state. Under metal-rich conditions the formation energies for interstitials and antisites are at least 3.8 eV larger than for the lowest neutral vacancy. Under oxygen-rich conditions the difference is smaller but even for the most favorable case (O on Ti antisite at point D in Fig. 1) the energy difference is at least 0.9 eV. In the following we therefore neglect interstitials and antisites and focus exclusively on vacancy defects. It should be pointed out that both metal and oxygen interstitials can play important roles in several other oxides with more open lattice structures (e.g., TiO_2, ZnO, SnO_2). In the case of perovskite lattices the interstitial sites are, however, much smaller and interstitials lead to significant strains which cause large formation energies.

The Brillouin zone integrations were carried out using a nonshifted $2\times2\times2$ Γ-centered mesh which, depending on the symmetry of the defect configuration, is equivalent to 4–6 k-points in the irreducible wedge of the Brillouin zone. The plane wave cutoff energy was set to 500 eV.

DFT calculations of point defect formation energies in semiconductors are subject to certain shortcomings, which in order to obtain physically meaningful results must be properly taken into account.[55,56] Although the band gap is typically underestimated, energy differences within the valence band and conduction bands, respectively, are usually rather well described. A simple correction of the band structure is, therefore, obtained by rigidly shifting the valence band (ΔE_{VB}) and the conduction band (ΔE_{CB}) with respect to each other. The correction energy is then given by

$$\Delta E_{bg} = n_e \Delta E_{\mathrm{CB}} + n_h \Delta E_{\mathrm{VB}}. \tag{2}$$

For a given defect and charge state the number of electrons in the conduction band n_e was determined by integrating the number of occupied conduction band states. The number of holes in the valence band n_h was similarly obtained as the number of empty valence band states. It should be noted that this correction only considers the effect of the band gap error on the band energy and assumes rigid levels. It does not take into account electronic relaxations which occur if self-interaction effects are properly included.

As experimentally the band gap of cubic $BaTiO_3$ cannot be determined for $T\rightarrow0$ K due to the ferroelectric phase transition, we estimated its value by extrapolation of the data at higher temperatures which yields $E_G^{\mathrm{expt}}=3.4$ eV (compare Fig. 10 in Ref. 38). In order to be able to correct for the underestimation of the band gap, we further assumed the offset of the calculated band structure to be restricted to the conduction band, i.e., $\Delta E_{\mathrm{VB}}=0$ and $\Delta E_{\mathrm{CB}}=E_G^{\mathrm{expt}}-E_G^{\mathrm{calc}}$.

Due to the use of supercells elastic and electrostatic interactions between the periodic images of the defects need to be taken into account.[55,57] Elastic interactions scale inversely with the volume, $\mathcal{O}(V^{-1})$, and therefore, have been corrected using finite-size scaling. For charged defects electrostatic interactions due to the net charge moment are present. The corresponding correction term can be expressed in the form of a multipole expansion.[57] The leading term, which describes monopole–monopole interactions, scales with $V^{-1/3}$ and can be calculated explicitly. The next term is due to monopole–quadrupole interactions. It scales with V^{-1} and can in principle also be evaluated explicitly. As it displays the same scaling behavior as the elastic interactions, it is, however, conveniently corrected using the same finite-size scaling procedure.[55,57,58] In addition, the latter approach has the advantage to avoid ambiguities in the calculation of the moments of the net charge distribution. It also allows to assess the reliability of the correction by means of the error of the linear extrapolation of the data. For strongly delocalized excess charge distributions higher order terms might become important which has, however, not been observed in the present calculations.

As the magnitude of the electrostatic interactions in condensed matter is screened, the monopole–monopole correction term requires knowledge of the static dielectric constant. For reasons of consistency the latter should be taken from first-principles calculations as well. Using a similar approach as in the present work Ghosez *et al.*[3] obtained an average value of $\varepsilon=57$ for barium titanate,[59] which was used in the present work.

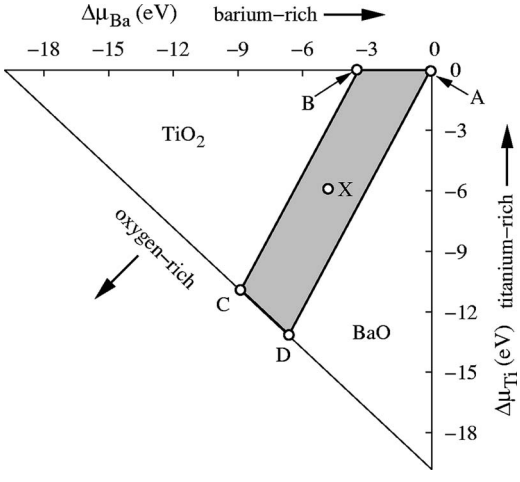

FIG. 1. Stability diagram for cubic barium titanate as determined from density-functional theory calculations. The area confined between points A, B, C, and D is the chemical stability range of $BaTiO_3$. The line through points C and D corresponds to maximally oxygen-rich conditions and an oxygen chemical potential of $\Delta\mu_{\mathrm{O}}=0$ eV. Along lines parallel to C–D the oxygen chemical potential is constant. The most negative value of $\Delta\mu_{\mathrm{O}}=\Delta H_f/3=-6.61$ eV is obtained in the upper right corner of the diagram.

2. Transition energies

If the formation energies of a given defect in charge states q_1 and q_2 are known, the thermal (equilibrium) transition level can be obtained according to

$$\varepsilon = -\frac{\Delta E_D^f(q_1) - \Delta E_D^f(q_2)}{q_1 - q_2}, \tag{3}$$

where $\Delta E_D^f(q_1)$ and $\Delta E_D^f(q_2)$ denote the formation energies at the valence band maximum for charge states q_1 and q_2, respectively.

3. Migration energies

The migration barriers for single vacancies (V_{O}, V_{Ba}, V_{Ti}) were calculated employing 40-atom supercells equivalent to $2\times2\times2$ unit cells. Brillouin zone integrations were carried out using the same k-point grids as for the formation energy calculations and the plane wave cutoff energy was again 500 eV. In order to obtain the saddle points, we applied the climbing image nudged elastic band method[60,61] which imposes a minimal number of constraints on the transition path. Only jumps between nearest neighbor sites were considered.

Unlike formation energies migration energies are obtained by calculating differences between configurations which are structurally and electronically very similar. As discussed in detail in Ref. 62 the calculation of migration barriers is, therefore, much less sensitive to the errors described in the foregoing section. For this reason, comparably small

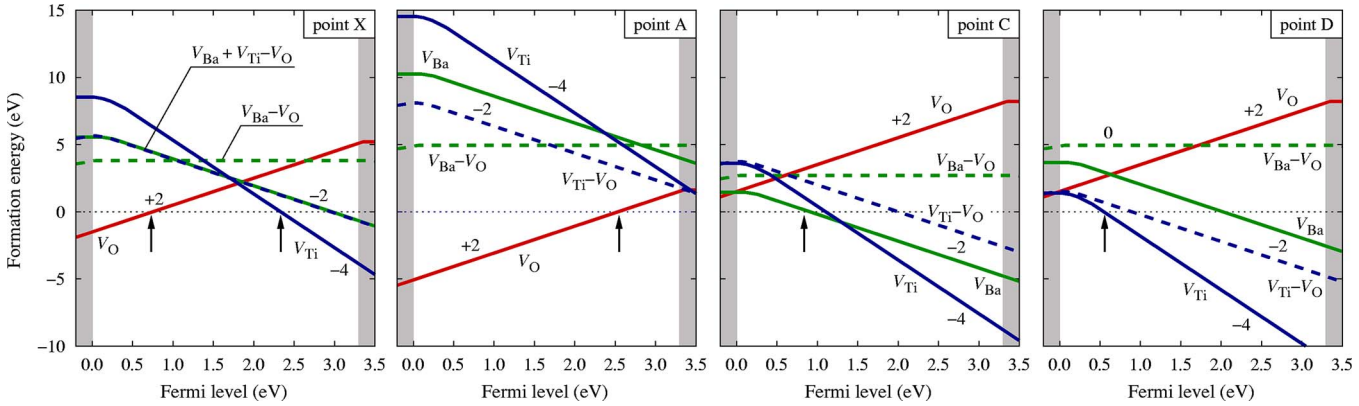

FIG. 2. (Color online) Variation of defect formation energies with Fermi level for representative thermodynamic conditions indicated in Fig. 1. The numbers indicate the charge states. Parallel lines correspond to identical charge states. The solid and dashed lines correspond to mono- and di-vacancies, respectively. The arrows indicate the position of the Fermi level pinning energy under different conditions.

supercells should be sufficient and due to the similar electronic structure band gap and potential corrections need not be applied.

III. RESULTS

A. Band structure

In agreement with full potential-linearized augmented plane wave[35] and pseudopotential plane wave calculations,[48] our results predict the valence band maximum (VBM) to be located at the *R*-point. On the other hand, in previous tight-binding linear muffin-tin orbitals calculations[36] within the atomic-sphere approximation the VBM was located at the Γ-point. In all of these calculations the difference between the highest occupied levels at *R* and Γ was calculated to be on the order of 0.1 eV or less. The effective masses of electrons and holes at the Γ-point, which can be used for instance for a self-consistent determination of the Fermi level and the charge carrier concentrations,[63] are given in Table I.

B. Chemical potentials and stability diagram

In order to be able to derive defect formation energies from total energy calculations, the thermodynamic reservoirs need to be defined. This requires knowledge of the cohesive energies of the constituents in their most stable conformation. Further, as the stability range of barium titanate is restricted by the formation of competing phases such as TiO_2 or BaO, the formation energies of these compounds have to be computed as well (see Sec. II B 1). The results of our calculations of the fully relaxed structures are compiled in Table II in comparison with experimental data. The overall agreement with the reference data is good. In particular, the calculated formation energies compare well with experimental data.

The range within which the chemical potentials of Ba, Ti, and O can vary is restricted by the condition

$$\Delta\mu_{Ba} + \Delta\mu_{Ti} + 3\Delta\mu_O = \Delta H_f[BaTiO_3], \tag{4}$$

which determines the outer triangle in the phase diagram shown in Fig. 1. Considering the compounds given in Table II, the chemical potentials are further subject to the following constraints:

$$\Delta\mu_{Ba} + \Delta\mu_O \leq \Delta H_f[BaO],$$

$$\Delta\mu_{Ba} + 2\Delta\mu_O \leq \Delta H_f[BaO_2],$$

$$\Delta\mu_{Ti} + 2\Delta\mu_O \leq \Delta H_f[TiO_2].$$

They confine the stability range of $BaTiO_3$ to the gray shaded area in Fig. 1. Repeating this analysis with the experimental data gives a phase diagram in good agreement with the calculated one.

C. Defect formation energies

The results of our calculations for the formation energies are summarized in Table III which shows the formation energies of mono- and di-vacancies for a Fermi level at the valence band maximum [E_F=0 eV in Eq. (1)] and for four representative combinations of chemical potentials, which are indicated in Fig. 1. The variation with the Fermi level is shown for the same four cases in Fig. 2. Due to the large formation enthalpy of $BaTiO_3$ the formation energies vary strongly between the extremal points of the phase diagram. In the metal-rich limit (along A–B) oxygen vacancies prevail. They have comparably small formation energies and therefore should be abundant defects. In both cases the formation energies become negative for some Fermi level which determines the so-called pinning energy, ε_{pin}. This implies that under equilibrium conditions the material cannot assume a Fermi level which is closer to the valence band maximum than ε_{pin}.[67] In the oxygen-rich limit either barium (point C) or titanium vacancies (point D) dominate. Fermi level pinning now occurs in the vicinity of the conduction band, which implies that the Fermi level cannot be pushed arbitrarily close to the conduction band minimum.

The equilibrium defect transition levels can be deduced from the formation energies using Eq. (3). They are presented in an effective band scheme in Fig. 3. As vacancies occur in their nominal charge states (V_{Ti}'''', V_{Ba}'', $V_O^{\cdot\cdot}$) almost over the entire band gap, only the band edges are shown. With regard to the effect of the band gap correction term given by Eq. (2), it turns out that if no band gap corrections are applied the donor transition levels ($q>0$) are near the *calculated* conduction band edge, whereas they are near the

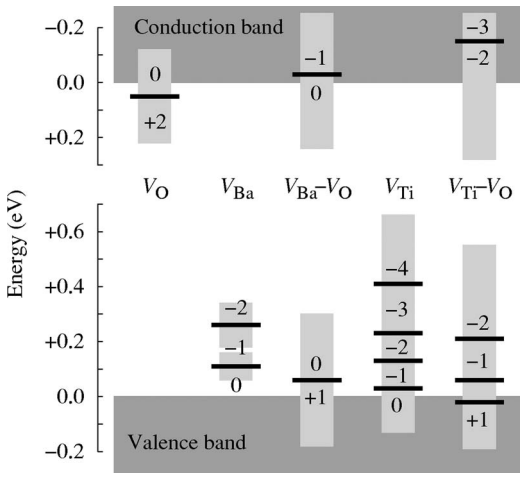

FIG. 3. Transition levels for mono- and di-vacancies in $BaTiO_3$. Only the band edges are shown. The dashed transition levels are positioned inside the valence or the conduction bands (indicated by the light gray shaded areas) and are only included for illustration. The dark gray shaded areas indicate the sum of the extrapolation errors for each transition.

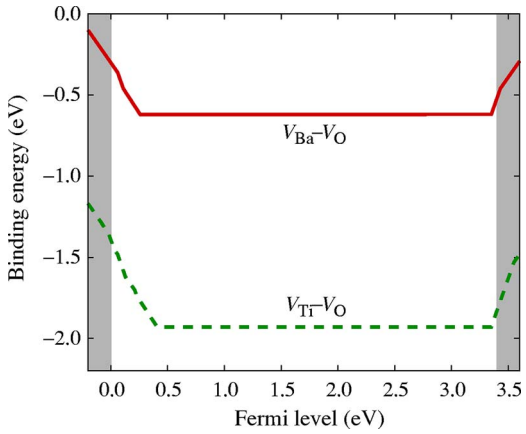

FIG. 4. (Color online) Binding energies for $V_{Ba}-V_O$ and $V_{Ti}-V_O$ divacancies as a function of Fermi level. The kinks correspond to charge transition points of the isolated defects (compare Fig. 2 and Fig. 3).

experimental conduction band edge if the corrections are included. This consistency indicates that the application of the band gap correction described in Ref. 56 is reasonable in the present case.

The location of the levels near the band edges is in agreement with several models which have been developed to reproduce the experimental data (see e.g., Refs. 8–12). It is evident from the extrapolation errors in Table III that typically DFT calculations cannot predict transition levels with an accuracy better than approximately 0.1 eV. However, even taking into account this limitation the present results show clearly the intrinsic defect levels to be very close to the band edges ($\lesssim$0.4 eV). In particular, this applies for the titanium vacancy for which, based on more simplistic calculations, the defect level has been previously calculated to be located −1.14 eV below the conduction band maximum.[54] A finding which is confuted by the present results.

The binding energy of a di-vacancy is given by the difference between its formation energy and the formation energies of the isolated mono-vacancies. It is therefore independent of the chemical potentials. As charge transitions occur only within about 0.4 eV of the band edges (see Fig. 3), the Fermi level position has very little influence (see Fig. 4). Over the widest range of the band gap the binding energy of the $V_{Ti}-V_O$–di-vacancy is $E_b=-1.93$ eV, whereas the value for the $V_{Ba}-V_O$–di-vacancy is $E_b=-0.62$ eV. Only near the band edges the attraction is somewhat reduced. Thus, the association of metal and oxygen vacancies is energetically strongly favored, especially in the case of the $V_{Ti}-V_O$–di-vacancy.

Note that the formation energy of the $V_{Ba}-V_O$–di-vacancy is constant along lines which are parallel to A–D in the phase diagram (Fig. 1) corresponding to the reaction $BaTiO_3+[V_{Ba}-V_O]\rightarrow TiO_2$. Equivalently, along lines parallel to B–D the sum of the formation energies of oxygen vacancies and $V_{Ti}-V_O$–di-vacancies is constant, $(BaTiO_3+[V_{Ti}-V_O]+V_O\rightarrow BaO)$.

D. Migration energies

The calculated migration barriers are compiled in Table IV. The smallest migration energies are obtained for oxygen vacancies and display a weak charge state dependence. Experimentally the migration barrier for oxygen vacancies has been determined to be $\Delta H_m=0.91$ (Ref. 20). The calculations compare well with this value. In particular, the barrier for the doubly positive charge state, in which the oxygen vacancy should occur for a Fermi level in the middle of the band gap, is in very good agreement with this reference value. We point out that the migration barriers for the different charge states of the oxygen vacancy are very similar to the values for cubic lead titanate calculated by Park within DFT.[28]

Using the Einstein relation $6D\tau=\langle r^2\rangle$, one can estimate the temperature above which a defect becomes mobile by determining the temperature for which $6D\tau$ exceeds $\sqrt{\langle r^2\rangle_{min}}$ (compare Refs. 62 and 68). The prefactor for the defect diffusivity can be approximated by the lowest optical phonon mode at the Γ-point which gives $\Gamma_0\approx 5$ THz (Ref. 3). If one assumes a typical isochronal annealing time of $\tau=10$ min and a mean defect separation between $\sqrt{\langle r^2\rangle_{min}}=100$ and 1000 nm, one arrives at the values which are given in the last column of Table IV. Obviously the only defects, which are fully mobile at typical processing temperatures, are oxygen

TABLE IV. Calculated migration energies of mono-vacancies in units of electron volts. The temperature ranges above which the defects become mobile are given in the last column. The negative charge states of the titanium vacancy were not considered as already the neutral charge state displays a huge barrier and, following the trends for the barium and oxygen vacancies, the addition of electrons can only be expected to further increase this value.

Defect	Charge	Barrier	Onset of mobility (K)
V_{Ba}	0	5.82	>2500
	−1	5.96	>2600
	−2	6.00	>2600
V_{Ti}	0	9.84	>4300
V_O	0	1.12	490–590
	+1	0.97	420–510
	+2	0.89	390–480

vacancies. In contrast, due to their very large activation barriers, the migration of metal vacancies is much lower even at temperatures close to the melting point (~1900 K, Ref. 65).

IV. DISCUSSION

Experimentally, at low oxygen partial pressures (*n*-type region) and high temperatures (~1300–1500 K) the dependence between the electrical conductivity and the oxygen partial pressure is found to be $p_{O_2}^{-1/6}$ which has been assigned to doubly charged oxygen vacancies.[8–12] In accordance the present calculations predict oxygen vacancies to be by far the most important defect under metal-rich conditions (low oxygen partial pressure) and to occur in charge state 2+ almost over the entire band gap. At somewhat lower temperatures ($\lesssim$1300 K) a transition to a $p_{O_2}^{-1/4}$ dependence is observed. At least two different explanations have been discussed in the literature.[8–10] Either (1) the charge state of the oxygen vacancies changes from 2+ to 1+ or (2) accidental acceptor dopants are present in the material. In order for the first explanation to be valid, the 2+/1+ transition level of the oxygen vacancy should be located 1.3 eV below the conduction band minimum.[8] However, as the present calculations locate this transition just 0.1 eV below the conduction band minimum, they provide support for accidental acceptor doping as the cause for the change in slope. In fact, a more detailed investigation of the relation between the conductivity and the oxygen partial pressure shows that this mechanism can also explain the $p_{O_2}^{1/4}$ dependence observed for higher oxygen partial pressures ($p_{O_2} \gtrsim 10^{-2}$ atm, *p*-type region).[63]

The structural and energetic differences between the para-electric, cubic phase, and the ferroelectric phases play a crucial role in determining the magnitude and the temperature dependence of ferroelectricity. As $BaTiO_3$ ceramics are typically processed at temperatures above the cubic–tetragonal phase transition (T_c=393 K) and as the onset of mobility ranges given in Table IV exceed this temperature, the point defect equilibria, which are established during cooling should correspond to the cubic phase. In particular, initially (prior to aging, see Refs. 15 and 16) oxygen vacancies should be rather randomly distributed over the symmetrically inequivalent oxygen lattice sites, even if a clear energetic preference exists for a particular lattice site (which is for instance the case for "*c*-site" vacancies in tetragonal lead titanate[23,69]). In addition, due to the large energy barriers for metal vacancy migration the distribution of barium and titanium, which is established during growth, is expected to be largely maintained if the material undergoes ferroelectric phase transitions.

The binding energies for di-vacancies are negative and large which implies a strong chemical driving force for their formation. As the migration barriers for metal vacancies are large, they are virtually immobile. In contrast, oxygen vacancies are very mobile at temperatures $\gtrsim$500 K. Thus, formation of di-vacancies should occur readily at typical growth temperatures by metal vacancies "capturing" diffusing oxygen vacancies.

Defect complexes such as di-vacancies or impurity-vacancy associates carry a dipole moment (see e.g., Ref. 30 for a quantitative calculation). On a cubic lattice different orientations of these defect dipoles are energetically degenerate. In the presence of an electric field[15,16] or for noncubic lattices[70] this degeneracy is, however, lifted (i.e., the energies for di-vacancy pairs, e.g., oriented along the [001] and [100] axes differs). As argued previously, depending on the barriers, the transition temperature and the cooling rate defect dipoles might not have enough time to achieve the orientation with the lowest energy. As metal vacancies are rather immobile, reorientation of these dipoles is much more likely to occur by oxygen vacancy jumps. The gradual reorientation of defect dipoles is then determined by the barrier for oxygen vacancy jumps in the first neighborhood of metal vacancies.

V. CONCLUSIONS

The thermodynamics and kinetics of vacancy defects in paraelectric cubic barium titanate have been studied by means of density functional theory calculations. First, formation, binding and migration energies were derived properly accounting for the shortcomings of the DFT method. The binding energies of metal-oxygen di-vacancies are found to be negative implying that in equilibrium under metal-rich (oxygen-rich) conditions all metal (oxygen) vacancies are bound in di-vacancy clusters. Although metal vacancies are practically immobile at realistic conditions, oxygen vacancies can readily migrate at typical growth temperatures. Di-vacancies can, therefore, form if metal vacancies capture one oxygen vacancy.

It is further confirmed that mono-vacancies occur in their nominal (ionic) charge states (V_{Ti}'''', V_{Ba}'', $V_O^{\cdot}$) over the widest range of the band gap. The dominant charge states for the di-vacancies are $(V_{Ti}-V_O)''$ and $(V_{Ba}-V_O)^{\times}$. Intrinsic defect levels are confined to a region within ~0.4 eV of the band edges. This is partially at variance with earlier calculations based on a more simplistic model, which suggested titanium vacancies to act as hole traps.[54]

The temperatures at which defects are immobilized are higher than or similar to the cubic–tetragonal phase transition temperature. The principal findings of the present study with respect to the thermodynamic behavior of mono- and di-vacancies are therefore also relevant for the initial defect distribution in the ferroelectric phases.

ACKNOWLEDGMENT

This project was funded by the *Sonderforschungsbereich 595* "Fatigue in functional materials" of the Deutsche Forschungsgemeinschaft.

[1] R. E. Cohen, Nature (London) **358**, 136 (1992).
[2] W. Zhong, D. Vanderbilt, R. D. King-Smith, and K. Rabe, Ferroelectrics **164**, 291 (1995).
[3] P. Ghosez, X. Gonze, and J. P. Michenaud, Ferroelectrics **194**, 39 (1997).
[4] S. Tinte, M. Stachiotti, M. Sepliarsky, R. Migoni, and C. Rodriguez, Ferroelectrics **237**, 41 (2000).
[5] D. M. Smyth, *The Defect Chemistry of Metal Oxides* (Oxford University Press, New York, 2000), Chap. 14.
[6] M. Fukunaga, G. Li, Y. Uesu, and K. Kohn, Ferroelectrics **286**, 79 (2003).
[7] A. Tombak, J. P. Maria, F. Ayguavives, Z. Jin, G. T. Stauf, A. I. Kingon, and A. Mortazawi, IEEE Microw. Wirel. Compon. Lett. **12**, 3 (2002).
[8] J. Daniels and K. H. Härdtl, Philips Res. Rep. **31**, 489 (1976).
[9] N. G. Eror and D. M. Smyth, J. Solid State Chem. **24**, 235 (1978).

[10]N. H. Chan, R. K. Sharma, and D. M. Smyth, J. Am. Ceram. Soc. **64**, 556 (1981).
[11]N. H. Chan, R. K. Sharma, and D. M. Smyth, J. Am. Ceram. Soc. **65**, 167 (1982).
[12]N. H. Chan and D. M. Smyth, J. Am. Ceram. Soc. **67**, 285 (1984).
[13]C.-R. Song and H.-I. Yoo, Solid State Ionics **120**, 141 (1999).
[14]C.-R. Song and H.-I. Yoo, Phys. Rev. B **61**, 3975 (2000).
[15]H. Neumann and G. Arlt, Ferroelectrics **76**, 303 (1987).
[16]G. Arlt and H. Neumann, Ferroelectrics **87**, 109 (1988).
[17]W. L. Warren, D. Dimos, B. A. Tuttle, G. E. Pike, R. W. Schwartz, and D. C. McIntyre, J. Appl. Phys. **77**, 6695 (1995).
[18]L. He and D. Vanderbilt, Phys. Rev. B **68**, 134103 (2003).
[19]W. Li, J. Ma, K. Chen, D. Su, and J. S. Zhu, Europhys. Lett. **72**, 131 (2005).
[20]W. L. Warren, K. Vanheusden, D. Dimos, G. E. Pike, and B. A. Tuttle, J. Am. Ceram. Soc. **79**, 536 (1996).
[21]D. J. Keeble, B. Nielsen, A. Krishnan, K. G. Lynn, S. Madhukar, R. Ramesh, and C. F. Young, Appl. Phys. Lett. **73**, 318 (1998).
[22]S. Zafar, R. E. Jones, B. Jiang, B. White, P. Chu, D. Taylor, and S. Gillespie, Appl. Phys. Lett. **73**, 175 (1998).
[23]C. H. Park and D. J. Chadi, Phys. Rev. B **57**, R13961 (1998).
[24]S. Pöykkö and D. J. Chadi, Phys. Rev. Lett. **83**, 1231 (1999).
[25]S. Pöykkö and D. J. Chadi, Appl. Phys. Lett. **75**, 2830 (1999).
[26]S. Pöykkö and D. J. Chadi, J. Phys. Chem. Solids **61**, 291 (2000).
[27]S. Pöykkö and D. J. Chadi, Appl. Phys. Lett. **76**, 499 (2000).
[28]C. H. Park, J. Korean Phys. Soc. **42**, S1420 (2003).
[29]C. Duque and A. Stashans, Physica B **336**, 227 (2003).
[30]E. Cockayne and B. P. Burton, Phys. Rev. B **69**, 144116 (2004).
[31]A. Shigemi and T. Wada, Jpn. J. Appl. Phys., Part 1 **43**, 6793 (2004).
[32]A. Shigemi and T. Wada, Jpn. J. Appl. Phys., Part 1 **44**, 8048 (2005).
[33]A. R. Allnatt and A. B. Lidiard, *Atomic Transport in Solids* (Cambridge University Press, Cambridge, 2003).
[34]M. Uludogan, T. Çagin, and W. A. Goddard III, in *Perovskite Materials*, edited by A. Navrotsky, K. R. Poeppelmeier, and R. M. Wentzcovitch (Materials Research Society, Pittsburgh, 2002), Vol. 718, p. D10.1.
[35]H. Salehi, S. M. Hosseini, and N. Shahtahmasebi, Chin. J. Physiol. **42**, 619 (2004).
[36]S. Saha, T. P. Sinha, and A. Mookerjee, Phys. Rev. B **62**, 8828 (2000).
[37]J. H. Rose, J. R. Smith, F. Guinea, and J. Ferrante, Phys. Rev. B **29**, 2963 (1984).
[38]S. H. Wemple, Phys. Rev. B **2**, 2679 (1970).
[39]G. Kresse and J. Hafner, Phys. Rev. B **47**, 558 (1993).
[40]G. Kresse and J. Hafner, Phys. Rev. B **49**, 14251 (1994).
[41]G. Kresse and J. Furthmüller, Phys. Rev. B **54**, 11169 (1996).
[42]G. Kresse and J. Furthmüller, Comput. Mater. Sci. **6**, 15 (1996).
[43]P. E. Blöchl, Phys. Rev. B **50**, 17953 (1994).
[44]G. Kresse and D. Joubert, Phys. Rev. B **59**, 1758 (1999).
[45]D. M. Ceperley and B. J. Alder, Phys. Rev. Lett. **45**, 566 (1980).
[46]J. P. Perdew and A. Zunger, Phys. Rev. B **23**, 5048 (1981).
[47]J. P. Perdew, K. Burke, and M. Ernzerhof, Phys. Rev. Lett. **77**, 3865 (1996); **78**, 1396(E) (1997).
[48]P. Ghosez, X. Gonze, and J. P. Michenaud, Ferroelectrics **220**, 1 (1999).
[49]Z. Wu, R. E. Cohen, and D. J. Singh, Phys. Rev. B **70**, 104112 (2004).
[50]G.-X. Qian, R. M. Martin, and D. J. Chadi, Phys. Rev. B **38**, 7649 (1988).
[51]S. B. Zhang, S.-H. Wei, and A. Zunger, J. Appl. Phys. **83**, 3192 (1998a).
[52]S. B. Zhang, S.-H. Wei, A. Zunger, and H. Katayama-Yoshida, Phys. Rev. B **57**, 9642 (1998b).
[53]Y.-J. Zhao, C. Persson, S. Lany, and A. Zunger, Appl. Phys. Lett. **85**, 5860 (2004).
[54]G. V. Lewis and C. R. A. Catlow, J. Phys. Chem. Solids **47**, 89 (1986).
[55]P. Erhart, K. Albe, and A. Klein, Phys. Rev. B **73**, 205203 (2006).
[56]C. Persson, Y.-J. Zhao, S. Lany, and A. Zunger, Phys. Rev. B **72**, 035211 (2005).
[57]G. Makov and M. C. Payne, Phys. Rev. B **51**, 4014 (1995).
[58]J. Lento, J.-L. Mozos, and R. M. Nieminen, J. Phys.: Condens. Matter **14**, 2637 (2002).
[59]E. Cockayne, J. Eur. Ceram. Soc. **23**, 2375 (2003).
[60]G. Henkelman, G. Jóhannesson, and H. Jónsson, *Methods for Finding Saddlepoints and Minimum Energy Paths in Progress on Theoretical Chemistry and Physics* (Kluwer Academic, Dordrecht, The Netherlands, 2000), p. 269.
[61]G. Henkelman, B. P. Uberuaga, and H. Jónsson, J. Chem. Phys. **113**, 9901 (2000).
[62]P. Erhart and K. Albe, Phys. Rev. B **73**, 115207 (2006).
[63]P. Erhart and K. Albe, Phys. Rev. B (in press).
[64]C. Kittel, *Introduction to Solid State Physics*, 8th ed. (Wiley, New York, 2004).
[65]*Handbook of Chemistry and Physics*, 85th ed., edited by D. R. Lide (CRC Press, Boca Raton, 2004).
[66]A. Every and A. McCurdy, *Landolt-Börnstein: Numerical Data and Functional Relationships in Science and Technology, New Series* (Springer, Heidelberg, 1992), Vol. III/29A.
[67]S. B. Zhang, S.-H. Wei, and A. Zunger, Phys. Rev. Lett. **84**, 1232 (2000).
[68]P. Ehrhart, P. Jung, H. Schultz, and H. Ullmaier, *Landolt-Börnstein: Numerical Data and Functional Relationships in Science and Technology, New Series* (Springer, Heidelberg, 1991), Vol. III/25.
[69]P. Erhart, R.-A. Eichel, P. Träskelin, and K. Albe (unpublished).
[70]H. Meštrić, R.-A. Eichel, T. Kloss, K.-P. Dinse, S. Laubach, S. Laubach, P. C. Schmidt, K. A. Schönau, M. Knapp, and H. Ehrenberg, Phys. Rev. B **71**, 134109 (2005).